JOURNAL OF GEOPHYSICAL RESEARCH, VOL. 114, B09404, doi:10.1029/2008JB005986, 2009

Predicting stress distributions in fold-and-thrust belts and accretionary wedges by optimization

P. Souloumiac,[1] Y. M. Leroy,[2] B. Maillot,[3] and K. Krabbenhøft[4]

Received 5 August 2008; revised 20 April 2009; accepted 19 May 2009; published 15 September 2009.

[1] The objective is to demonstrate that the equilibrium element method (EEM) provides the stress distribution in geometrical models of folds, relevant to fold-and-thrust belts as well as accretionary wedges. The core of the method, inherited from limit analysis, is the search for an optimum stress field that (1) is in equilibrium, (2) remains everywhere below or equal to the maximum strength of the rock, and (3) balances the largest possible applied tectonic force. This force and the associated stress field are interpreted as those at the onset of rupture. The method makes no appeal to the rock rheology nor to its elasticity, except for its maximum strength described here with the Coulomb criterion. The stress fields are discretized by elements covering the whole domain and allowing for discontinuities. The example chosen to illustrate the potential of the EEM and to validate our implementation is the thrusting of a rectangular sheet over a flat and weak décollement. The EEM reproduces the solution proposed by Hafner (1951) on the basis of linear elasticity, as long as the strength limit is not reached in the bulk of the domain. The EEM shows in addition that failure in the bulk prevents the activation of the décollement. The EEM is then applied to two fault-bend folds, with known ramp and flat décollement, with and without relief buildup. It is shown that the transition from the flat to the ramp hanging walls occurs through a narrow fan defining the back thrust. The predicted dip of this back thrust decreases with increase in the ramp friction angle, the relief buildup, as well as the ramp curvature. A sharp increase and then a sharp decrease in the magnitudes of the equivalent shear stress and of the mean stress are observed as one moves from the lower flat, through the back thrust up the ramp. If the ramp friction angle is too large, or the relief too important, the EEM predicts the initiation of a new thrust rooting at the back wall, instead of activating the proposed ramp. The application to detect the incipient thrust system within the toe of Nankai's accretionary wedge, southeast coast of Japan, is proposed in the auxiliary material.

Citation: Souloumiac, P., Y. M. Leroy, B. Maillot, and K. Krabbenhøft (2009), Predicting stress distributions in fold-and-thrust belts and accretionary wedges by optimization, *J. Geophys. Res.*, *114*, B09404, doi:10.1029/2008JB005986.

1. Introduction

[2] There are two drastically different approaches to capture the development of fault-bend folds in fold-and-thrust belts and accretionary prisms. The first line of study relies on numerical techniques, such as the finite element method (FEM), enforcing mechanical equilibrium in a weak sense and accounting for complex rock rheologies [*Erickson and Jamison*, 1995; *Erickson et al.*, 2001]. This line of work is an active area of research, requiring benchmarking among experts [*Buiter et al.*, 2006], because it meets several technical difficulties regarding the onset of discontinuities [*Ortiz et al.*, 1987] and their development into ramps. Also, the details of the elastic-plastic constitutive relations control the strain localization conditions [*Rudnicki and Rice*, 1975] but are difficult to interpret on the basis of field observations [*Leroy and Triantafyllidis*, 2000]. The second approach to capture fault-bend folds is purely geometrical and relies on simple rules to construct the fold development, based essentially on the experience of the field geologist or the seismic interpretor (see, e.g., *Suppe* [1983] for the fault-bend fold rules). The simplicity of the geometrical rules renders possible the systematic construction of complex structures which, completed by temperature predictions, have practical applications in the oil industry [*Zoetemeijer and Sassi*, 1992; *Sciamanna et al.*, 2004]. Furthermore, such geometrical modeling requires only a fraction of the computer time necessary for the FEM simulations. There is, however, no concrete and objective means to select between two possible geometrical models of folding in the absence of any account of material properties,

[1] Laboratoire MSS-Mat, École Centrale Paris, CNRS, Paris, France.
[2] Laboratoire de Géologie, École Normale Supérieure, CNRS, Paris, France.
[3] Département Géosciences Environnement, Université de Cergy-Pontoise, Cergy-Pontoise, France.
[4] Centre for Geotechnical and Materials Modeling, University of Newcastle, Callaghan, New South Wales, Australia.

0148-0227/09/2008JB005986$09.00

mechanical equilibrium, or tectonic force. We propose to apply a classical approach used in soil mechanics and geotechnics to alleviate this deficiency.

[3] In geotechnics, the critical load that will permanently damage a structure or a foundation is the prime objective. It can be determined by solving the full mechanical problem using the FEM, if the details of the constitutive rules of the materials are known. Alternatively, limit analysis provides bounds on the values of the critical load with few assumptions on the rheology [*Salençon*, 1974]. It proceeds in two parts: in the kinematics approach, an upper bound to the critical load is determined by finding possible failure geometries. In the statics approach, a lower bound is derived by constructing possible stress fields which balance the load without exceeding the material strength. In both cases, an optimization is carried out to obtain bounds as close as possible to each other. Since we deal here with upper crustal structures, the Coulomb criterion is well adapted to detect the onset of rock failure. It produces conveniently a convex strength domain in the appropriate stress space, a property required by the upper and lower bound theorems. Our interpretation of these theorems is different from the classical limit analysis, as applied by *Odé* [1960], in that a complete theory for perfectly plastic solids is not considered. In particular, the concept of flow rule, essential to define the plastic strain rate is not necessary in this contribution. The Coulomb criterion is the only element of rheology which is assumed.

[4] This work is part of a research effort to account for rock strength and mechanical equilibrium in geometrical models of fault-related folds by extension of the classical limit analysis. Among previous work, *Maillot and Leroy* [2006] proposed to extend the kinematics approach of classical limit analysis to the development of folds. The idea was further developed by *Cubas et al.* [2008], who studied a forward sequence of thrusting in an accretionary wedge. Note that the kinematics approach requires no rheology other than strength criteria (Coulomb again). It is based on velocity fields but the symmetric parts of their gradients are not related to any stress fields since no constitutive relations are postulated.

[5] Here we present a numerical implementation of the statics approach of limit analysis: the Equilibrium Element Method (EEM). The idea of the statics approach is to search within the set of statically admissible (SA) stress fields, (i.e., stress fields satisfying local mechanical equilibrium including potential discontinuities and balancing forces applied at the boundaries of the domain), the optimum field which respects the rock strength limit at every point of the domain [*Salençon*, 2002]. By optimum, we mean the stress field that balances the largest applied forces, which is a lower bound to the exact applied force at failure. Note that only stress is discussed with the statics approach and there is no attempt to deduce a velocity field, nor a displacement field, nor a displacement gradient or jump. The main difficulty of the statics approach is that analytical solutions for SA stress fields even in two dimensions are not easily constructed. One could consider polynomial expressions for an Airy stress function, as done typically for elasticity problems [*Hafner*, 1951], but the extension to complex geometries quickly becomes cumbersome. It is thus preferable to discretize the domain of interest, typically with triangular elements in a 2-D setting. In contrast to the displacement-based finite element method, the stress components are the nodal unknowns. The resulting equilibrium element method (EEM) provides a set of equalities and inequalities for the nodal unknowns which correspond to the equilibrium conditions and the necessity to satisfy the rock strength limits, respectively.

[6] Among the merits of the EEM, first, discontinuities are built in the mesh along the side of every triangle providing new results on the stress distribution of the studied structures. Second, the EEM requires only the knowledge of the material strength. For the Coulomb criterion the only parameters required to produce the stress field are the distribution of friction angle and cohesion over the structure. These two parameters are certainly more in line with the way of thinking of a field geologist then the complete set of parameters necessary to define an elastic-plastic material required for an FEM simulation. Third, the search for the optimum stress field is not computer-intensive and is realized with a small fraction of the time necessary to produce an increment of deformation with a FEM code [*Souloumiac and Modaressi*, 2008]. A clear limitation of the EEM is that it cannot predict substantial elastic or viscous deformations prior to failure since no elastic or viscous behavior is assumed.

[7] The paper contents are as follows. Section 2 contains a technical presentation of the EEM with the particular example of the sliding of a rectangular sheet over a flat horizontal décollement. Section 3 is devoted to the application of the EEM to two fault-bend folds. The first fold is permanently eroded and the second fold builds up relief. In both cases, it is shown that the transition from the flat region to the ramp hanging wall occurs with a failure mechanism having the shape of a narrow fan, referred to as the back thrust. The stress concentration due to the rooting of the ramp on the décollement and the presence of this back thrust determines the main characteristics of the stress field over the structure. A comparison of the EEM predictions to the finite difference results of *Gonzáles et al.* [2008] is also proposed. Text S1 in the auxiliary material gives additional details on our predictions and proposes an application to Nankai accretionary wedge, southeast coast of Japan.[1] It is shown that minute variations in the friction angle of the décollement and details of the topography largely control the position of the failure mechanism which could be composed of a single ramp with two parallel back thrusts or of two subparallel ramps.

2. EEM and Its Validation With Hafner's Problem

[8] The objective of this section is to introduce the EEM and to validate our implementation with the example of a rectangular sheet sliding over a flat décollement, a problem suggested by *Hafner* [1951] in a seminal contribution on overthrusting. The geometry of the domain Ω and the loading are presented in Figure 1. The loading over the left

[1] Auxiliary materials are available in the HTML. doi:10.1029/2008JB005986.

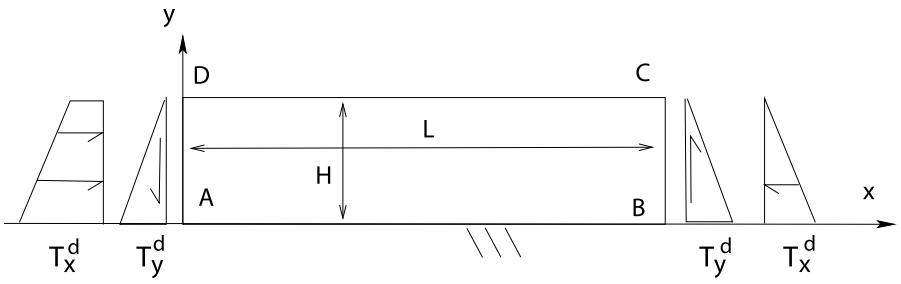

Figure 1. The geometry and the loading of the problem studied by *Hafner* [1951]. A 2-D rectangular block Ω (ABCD) of length L and thickness H, set along AB, the horizontal décollement, is subject to applied loads $\mathbf{T}^d$ at its vertical ends.

boundary AD has a normal and tangential component defined by

$$T_x^d = \rho g(H-y) + aL, \quad T_y^d = -a(H-y), \quad x = 0, \quad \forall y \in [0;H], \tag{1}$$

in which ρ, g are the material density, the gravity acceleration, acting in the y direction and in the negative sense, respectively, and a a positive scalar (unit Pa/m). The total horizontal force acting on the left boundary is

$$F(a) \equiv \int_A^D T_x^d(y)dy = \frac{1}{2}\rho g H^2 + aLH. \tag{2}$$

Along the right boundary BC, the two components of the distributed applied force are

$$T_x^d = -\rho g(H-y), \quad T_y^d = a(H-y), \quad x = L, \quad \forall y \in [0;H], \tag{3}$$

resulting in the total horizontal force on the right boundary equal to $\frac{1}{2}\rho g H^2$. The upper surface CD is stress free

$$T_x^d = T_y^d = 0, \quad \forall x \in [0;L], \quad y = H. \tag{4}$$

The domain boundary $\partial\Omega_T$ where forces are prescribed, and identified by the superscript d (data), is thus composed of the top free surface and the two lateral boundaries only. The décollement, having specific properties, is described as a material discontinuity in the following. Hafner's problem consists in determining the exact tectonic force (equation (2)) which triggers slip on the décollement or bulk failure. In this respect, a is the unknown of the problem.

2.1. Equilibrium Element Method

[9] The statics approach does not provide the exact solution to Hafner's problem. Instead, it seeks to establish a lower bound to the exact applied force. It proceeds in several steps: first, a stress field is constructed, by any means (analytical or numerical), that must be in equilibrium, and respect everywhere the maximum strength of the rock. Second, compute by quadrature as in (2), the applied load balanced by this field. It is a lower bound to the exact solution. The third step consists in optimizing the stress field to balance the largest possible applied load. In other words, the method provides the largest lower bound to the exact, unknown applied force at failure, and the corresponding optimum stress field over the domain. The equilibrium element method (EEM) follows this strategy, using a spatial discretization with elements to construct numerically the stress field, and dedicated algorithms to optimize it.

[10] The optimum stress field is searched among the set of statically admissible (SA) stress fields. Each element of this set satisfies mechanical equilibrium, requiring three conditions to be met. First, at every point within the bulk

$$\mathrm{div}(\boldsymbol{\sigma}) = -\rho\mathbf{g}, \quad \forall \mathbf{x} \in \Omega, \tag{5}$$

in which $\boldsymbol{\sigma}$ is the stress tensor. Bold letters identify tensorial or vectorial quantities. Second, across any potential discontinuity Λ of normal $\mathbf{n}$ within the domain Ω, the stress vector, defined by $\mathbf{T} = \boldsymbol{\sigma} \cdot \mathbf{n}$, must be continuous

$$[[\boldsymbol{\sigma}]] \cdot \mathbf{n} = \mathbf{0}, \quad \forall \mathbf{x} \in \Lambda, \tag{6}$$

in which the double brackets denote the difference between the stress on the two sides of the discontinuity ($[[\boldsymbol{\sigma}]] = \boldsymbol{\sigma}^+ - \boldsymbol{\sigma}^-$, the normal pointing to the + region). Third, the boundary conditions over $\partial\Omega_T$ must be satisfied, requiring

$$\boldsymbol{\sigma} \cdot \mathbf{n} = \mathbf{T}^d, \quad \forall \mathbf{x} \in \partial\Omega_T, \tag{7}$$

where $\mathbf{n}$ is the normal to the boundary at point $\mathbf{x}$. These boundary conditions are defined in (1), (3), and (4) for Hafner's problem.

[11] The SA stress field must also be such as not to overcome the strength of the material. For any discontinuity or fault of known orientation, the specific strength domain (linear in stress) is based on the Coulomb criterion. More specifically, for the décollement (line AB, Figure 1, with normal $\mathbf{n}(0, 1)$), the strength domain reads

$$\begin{aligned} &G_D(\boldsymbol{\sigma}) = \{\boldsymbol{\sigma} | \pm\tau + \sigma_n \tan\phi_D - c_D \le 0\} \\ &\text{with} \quad \sigma_n = \mathbf{n} \cdot (\boldsymbol{\sigma} \cdot \mathbf{n}), \quad \tau = \mathbf{m} \cdot (\boldsymbol{\sigma} \cdot \mathbf{n}), \end{aligned} \tag{8}$$

in the space spanned by the normal stress σ_n and the resolved shear stress τ. The vector $\mathbf{m}(-1, 0)$ is of unit norm

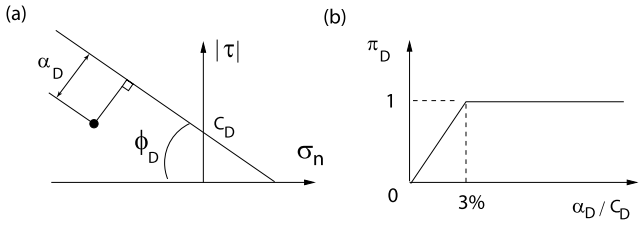

Figure 2. The definition of (a) the distance to the criterion and (b) of the scaled distance to the criterion are illustrated for the case of the décollement strength domain.

and tangential to the décollement. The parameters ϕ_D and c_D introduced in (8) are the friction angle and the cohesion of the décollement, respectively. In the bulk, the orientation of the failure plane is not specified and the strength domain (nonlinear in stress) is generalized to

$$\begin{aligned} G_B(\boldsymbol{\sigma}) &= \{\boldsymbol{\sigma} | \sigma_e + 2P\sin\phi_B - 2c_B\cos\phi_B \le 0\} \\ \text{with} \quad \sigma_e &= \sqrt{\left(\sigma_{xx}-\sigma_{yy}\right)^2 + 4\sigma_{xy}^2}\,, \quad P = \left(\sigma_{xx}+\sigma_{yy}\right)/2, \end{aligned} \tag{9}$$

in which ϕ_B and c_B are the friction angle and the cohesion of the bulk material, respectively. The stresses P and σ_e in (9) are referred to as the in-plane mean stress and the equivalent shear stress, respectively.

[12] It will be important in what follows to estimate the distance of the stress state to the boundary of the strength domain, i.e., the distance to failure. This concept is illustrated in Figure 2a where the distance to failure is denoted α_D at a given point on the décollement. Normal and tangential stresses at that point are marked by the solid dot. The distance, with unit of stress, is defined by

$$\alpha_D = (c_D - |\tau| - \sigma_n \tan\phi_D)\left(1+\tan^2\phi_D\right)^{-1/2}, \tag{10}$$

for the décollement and by

$$\alpha_B = (2c_B\cos\phi_B - \sigma_e - 2P\sin\phi_B)\left(1+4\sin^2\phi_B\right)^{-1/2}, \tag{11}$$

for any point in the bulk material according to the two definitions (8) and (9), respectively. It will be convenient to scale that parameter to concentrate our attention to very small distances to failure. For that purpose, the scaled distance to the criterion (Figure 2b) is proposed

$$\pi_b = \min\left(1, \frac{\alpha_b}{0.03\, c_b}\right), (b = B, D), \tag{12}$$

the value of 3% being chosen arbitrary.

[13] In summary, according to the statics approach, any SA stress field which satisfies pointwise the constraint of the convex strength domain (8) and/or (9) provides a lower bound to the exact tectonic force (2). However, the search within the set of SA stress fields for the optimum solution is difficult and the benefit of the EEM is to propose a systematic construction of SA stress fields by discretizing the domain. It is done in the spirit of the classical displacement-based finite element method (FEM) and we choose linear, three-noded triangular elements. The main difference, however, with the FEM is that within any element Ω^h, it is the stress which is interpolated linearly from the nodal values $\boldsymbol{\sigma}^i$

$$\boldsymbol{\sigma}(\mathbf{x}) = \sum_{i=1}^{3} N_i(\mathbf{x})\boldsymbol{\sigma}^i, \forall \mathbf{x} \in \Omega^h, \tag{13}$$

in which the superscript i is the local node number (1 to 3). The functions $N_i(\mathbf{x})$ are linear and take the value of one at node i and of zero at the other two nodes. Note that discontinuities, which equilibrium is presented by (6), are assumed to occur along the three sides of each triangle. The corresponding linear equilibrium equations, after discretization, are constructed elegantly by collapsing two triangular elements (zero surface) along each of theses three segments. The EEM construction is presented in more technical details than by *Krabbenhøft et al.* [2007] as well as in section 4 of Text S1. It suffices to know that the final set of equations is of the type

$$\begin{aligned} &\text{Max}(f)\{\sigma\}, \\ &\text{Subject to } [A]\{\sigma\} = \{b\}, \\ &\text{and } \boldsymbol{\sigma}^i \in G_b, \end{aligned} \tag{14}$$

where $\{\sigma\}$, (f) are the column vector containing all the nodal stress unknowns and the line vector associated to the loading to be optimized, respectively. Thus, the product $(f)\{\sigma\}$ is a scalar defining the magnitude of the applied load, for example it is $F(a)$ in (2). $[A]$ is the matrix resulting from the three equilibrium conditions (5), (6), and (7) with the discretization (13), constructed so that $[A]\{\sigma\}$ corresponds to the left-hand sides of (5), (6), and (7) and $\{b\}$, to the right-hand sides of (5), (6), and (7). The last equation in (14) stipulates that each nodal stress must satisfy the relevant strength condition (equation (8) or (9)). It is this optimization problem which is set up with the standard finite element code SARPP (Structural Analysis and Rock Physics Program, Ecole Normale Supérieure, Paris, 2007) and solved with the commercial package Mosek (version 5, optimization software, http://www.mosek.com, 2008) throughout the rest of this contribution.

2.2. Hafner's Solution

[14] The solution of Hafner's problem which is now presented is the exact, analytical solution and it is used to validate the numerical implementation of the system (14) in section 2.3.

[15] Equilibrium of external forces provides the two components of the total reaction force from the foundation along AB, Figure 1. The vertical component R_y is ρgHL and corresponds to the weight of the block Ω while the horizontal reaction R_x is $-aHL$ and results from the difference between the two horizontal forces on BC and AD, as can also be seen in Figure 1. The exact distribution of these two components of the reaction force over AB is not known but, if the décollement is fully activated, the resolved shear stress (assumed of same sign over the whole décollement) and the normal stress must satisfy pointwise the Coulomb criterion (8). Consequently, the two force components must

Table 1. Definition, Dimension and Value Selected for the Parameters of Hafner's Problem

Definition	Dimension	Value
Length L	km	0.5
Height H	km	0.2
Mass density ρ	kg/m^3	2300.
Gravity acceleration g	m/s^2	10.
Friction angle in the bulk ϕ_B	deg	30.
Cohesion in the bulk c_B	Pa	variable
Friction angle of the décollement ϕ_D	deg	15.
Cohesion of the décollement c_D	Pa	0

satisfy $-R_x - R_y \tan\phi_D = c_D L$, providing the expression for the maximum value of the basic unknown a:

$$a_D = \frac{c_D}{H} + \rho g \tan\phi_D, \tag{15}$$

the subscript D marking the fact that the whole décollement is activated. This result is valid if the loading generated for that specific value of a_D does not lead to rupture within the pristine material. To check that possibility, it is necessary to construct the stress state within the block Ω. Following *Hafner* [1951], the simplest SA stress state is

$$\begin{aligned} \sigma_{xx} &= -\rho g(H-y) - a(L-x), \\ \sigma_{yy} &= -\rho g(H-y), \\ \sigma_{xy} &= a(H-y). \end{aligned} \tag{16}$$

This field satisfies equilibrium (5), there is no discontinuity relevant for (6) and the stress vectors $\mathbf{T} = \boldsymbol{\sigma} \cdot \mathbf{n}$ for the outward normal $\mathbf{n}$ to the left, right and top boundaries of the domain are indeed equal to the applied force density defined in (1), (3) and (4), respectively. One shows further that the strength domain boundary is first reached in the bulk at the corner D. There, σ_{xx} is the only nonzero stress and the maximum value of the loading unknown a is then

$$a_B = \frac{2c_B}{L}\sqrt{k_P}, \quad \text{where} \quad k_P = \frac{1+\sin\phi_B}{1-\sin\phi_B} \tag{17}$$

is the passive Rankine's coefficient. The subscript B attached to the scalar a in (17) is to emphasize that failure occurs in the bulk.

[16] To capture the transition between the two modes of failure (décollement or bulk), it is proposed to define the critical bulk cohesion c_B^* for which $a_D = a_B$. This equality provides

$$c_B^* = \frac{1}{2\sqrt{k_P}}\left(c_D\frac{L}{H} + \rho g L \tan\phi_D\right). \tag{18}$$

It is expected that the EEM will select a_B in (17) or a_D in (15) for ratios c_B/c_B^* smaller and greater than one, respectively.

2.3. Optimized Solution

[17] The implementation of the EEM is now validated by comparing our predictions with the analytical solution. The values selected for the geometrical and material parameters are summarized in Table 1 (length and stress are scaled by L and $\rho g H$, respectively, in all numerical simulations). The mesh is composed of 30 × 20 regular rectangles, each composed of four crossed triangles.

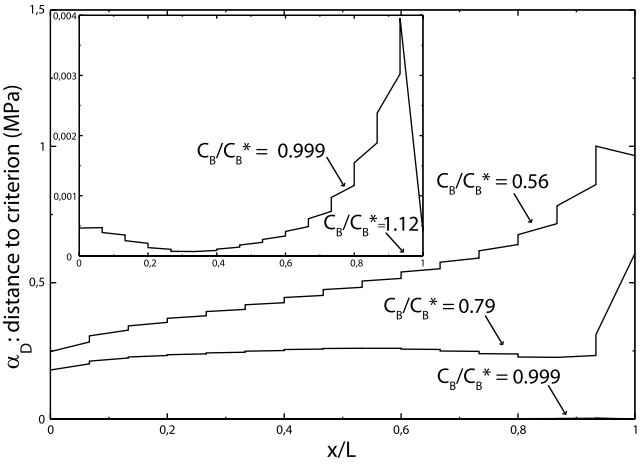

Figure 3. Distance to the criterion α_D over the décollement for different values of the ratio c_B/c_B^* according to the EEM for Hafner's problem. Note that the décollement is nowhere activated for ratios less than one.

[18] The force predicted by the EEM is presented in Table 2 and compared to the analytical expression (2) with a set to a_D (15) if $c_B > c_B^*$, and to a_B (17) otherwise (here, $c_B^* = 0.8895$ MPa). The conclusion is that the force is computed with an accuracy of six significant digits, validating partly our development. Figure 3 presents the distance to the criterion α_D, defined in (10), distributed over the décollement, for various values of the ratio c_B/c_B^*. The distance is zero and the whole décollement is indeed fully activated for $c_B/c_B^* = 1.12$. The transition to a partly activated décollement occurs for a ratio of one with an accuracy of five significant digits. For ratios smaller than one, the whole décollement is then deactivated. The patch closest to activation is at the coordinate $x = 0.3L$, inset of Figure 3.

[19] The predicted stress distributions are presented in Figures 4a and 4b for bulk failure and décollement activation, respectively. Although not visible in Figures 4a and 4b, bulk failure occurs at a single point, which is the top left corner of the domain, as predicted by Hafner. The σ_{xx} stress (Figure 4, top) has a vertical gradient which is linear at the right boundary because of the imposed condition $\sigma_{xx} = -\rho g(H-y)$. The vertical gradient is also positive along any vertical axis crossing the section. This gradient varies with the x coordinate nearly linearly, as can be seen by following

Table 2. Analytical and EEM Values of the Tectonic Force[a]

	Tectonic Force	
c_B/c_B^*	Theory (GN)	EEM (GN)
0.562	0.806410	0.806410
0.787	0.944974	0.944974
0.999	1.075917	1.075917
1.124	1.076288	1.076288

[a]For different values of the bulk cohesion c_B normalized with $c_B^* = 0.8895$ MPa. The two values agree up to six significant digits.

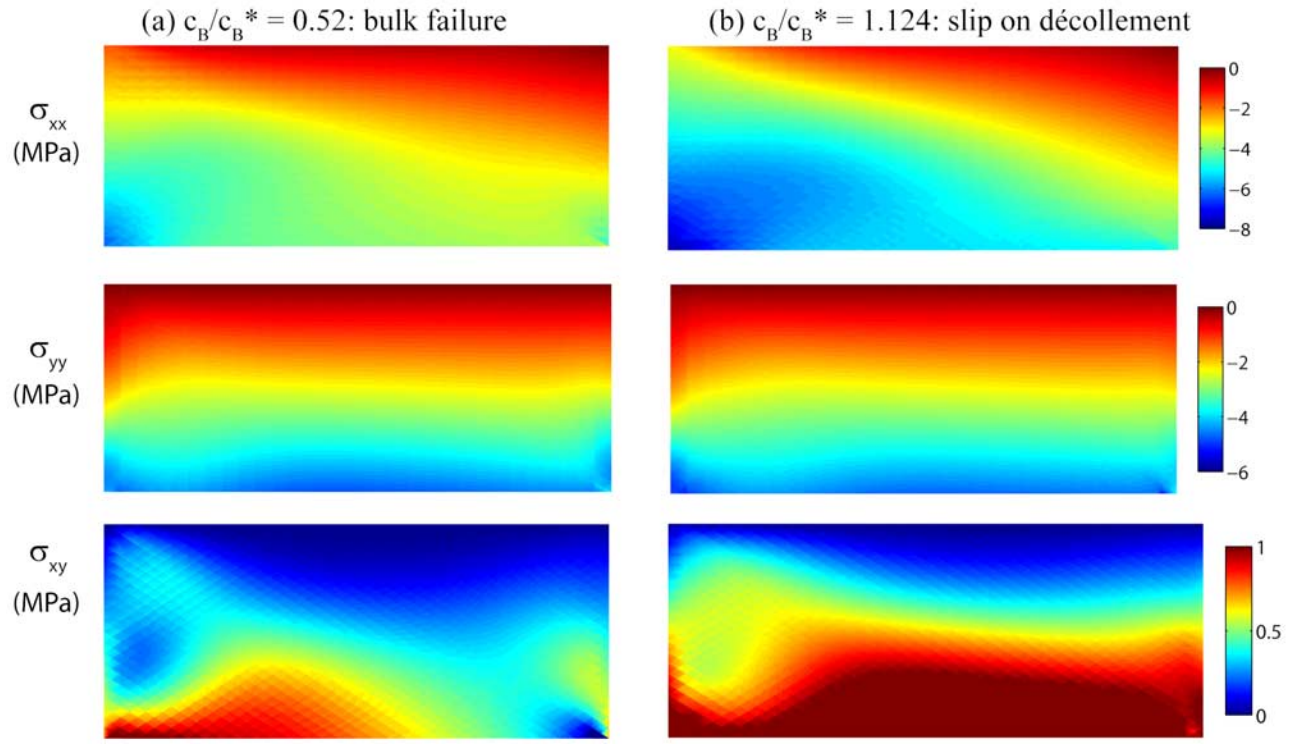

Figure 4. The three stress components (σ_{xx}, σ_{yy}, σ_{xy}) predicted with the EEM for Hafner's problem, for two values of the bulk cohesion. (a) Failure occurs in the bulk at the top left corner. (b) The whole décollement is activated. Only for $c_B = c_B^* = 0.8895$ do the two mechanisms get activated concurrently. Parameters are given in Table 1.

the yellow series, especially for case in Figure 4b. It corresponds then, approximately, to the elasticity solution presented in (16). The distribution of the blue contours (−5 MPa and smaller) shows, however, that the EEM selects a solution more complex than Hafner's for both bulk and décollement failure. The vertical stress distribution (Figure 4, middle) is driven by the gravity gradient, found analytically in (16), in the central part of the sheet for the two cases considered. However, this gradient is modified close to the left boundary. The shear stress (Figure 4, bottom) shows also a mainly vertical gradient in the central region but is affected with a horizontal gradient, especially along the left boundary if the décollement is activated. The intensity of the shear stress is very different in Figure 4a (bulk failure) from the one in Figure 4b (décollement activated). Note that the shear stress is nearly uniform on the décollement if activated. This is due to the uniform vertical stress and the requirement to satisfy Coulomb criterion in (8) over the whole décollement.

[20] A few comments concerning the method are now in order. Discontinuities in shear stress are observed at plus and minus 31°, corresponding to the sides of the triangles in every cell. Some of those are artifacts of the method which are worth to be presented to remind the reader that the stress interpolation is simply linear over each element. There are also a few horizontal jumps in σ_{xx} (left top corner of Figure 4a, top) and some vertical jumps in σ_{yy} (close to middepth of the left boundary of Figure 4a, middle, and 4b, middle).

[21] All those discontinuities are triggered by the EEM because the strong gradients are not resolved properly by the discretization. These results are a consequence of the discretization but not all discontinuities can be eliminated by refining the mesh and could be due to a discontinuity in the geometry or the loading, as in linear elasticity [*Timoshenko and Goodier*, 1934].

[22] To conclude this section, the implementation of the EEM has been validated by comparing the predicted forces and stress distribution with an analytical solution. The method captures exactly the tectonic force required to slide the block over the décollement or to initiate failure in the bulk. In the former case, the stress distribution is very close to the solution proposed by *Hafner* [1951] although no assumptions concerning the elasticity of the bulk material are necessary for the EEM. The elasticity solution and the EEM solution are both statically admissible and lead to the same best lower bound. The existence of two solutions in stress for the same best lower bound is not surprising since there is no proof of uniqueness. Consequently, despite the plausible interpretation of the results presented in Figure 4, it cannot be claimed that there exists no other SA stress field leading to the same bound on the tectonic force. This lack of uniqueness is classical in limit analysis [*Hill*, 1950].

[23] As a final remark, it should be noted that failure in the bulk and activation of the décollement are not two concomitant failure modes, except for $c_B = c_B^*$. *Hafner* [1951] assumed that the décollement was activated ($a = a_D$) and then used the stress field (16) to deduce the orientation

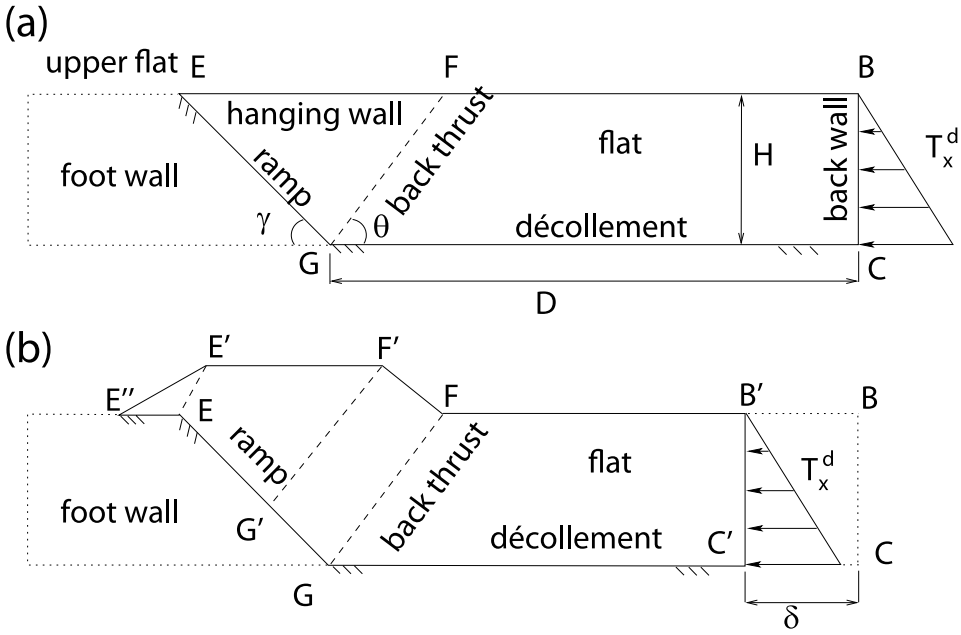

Figure 5. Geometry and terminology of the fault-bend fold. The compression along the back wall results in slip of the flat on the décollement, by δ toward the left. Material points crossing the back thrust (dip θ) are transported parallel to the ramp (dip γ). When crossing the initial surface (EF), they are (a) eroded or (b) build up relief. The tip of the hanging wall (E″E′E) is projected on the upper flat (EE″) assuming conservation of mass (i.e., area) and slips along it.

of potential fractures in the bulk. This seems inconsistent since (1) $c_B = c_B^*$ is a restrictive case and (2) onset of bulk failure is localized at the top left corner of the domain.

3. Stress in Fault-Bend Folds

[24] The objective is now to apply the EEM at different stages of the development of a fault-bend fold with or without erosion (Figure 5). The geometrical construction resulting in Figure 5b is based on the ideas presented by *Suppe* [1983] and the exact method is commented at length by *Cubas et al.* [2008]. It is not discussed here any further. We determine the optimum stress state at any stage of shortening δ, regardless of the history of the structure, considering the geometry as given. In particular, the upper flat, the décollement and the ramp are predefined and assumed to have specific properties. They are usually considered weaker than the bulk material. To the contrary, the back thrust is not introduced as a specific surface in the EEM simulations. One of our objective is to analyze the transition between the hanging wall and the flat and to let the EEM define the nature of the back thrust. Note that the tectonic force is defined for the EEM by the distributed horizontal force T_x^d (Figure 5). The vertical linear gradient of T_x^d is the only unknown of the problem. The vertical component of the distributed force T_y^d is set to zero.

[25] Material and geometrical parameters considered for those two examples are summarized in Table 3. Note that dimensionless length and stress are scaled by D and $\rho g D$, respectively (all simulations are based on dimensionless quantities identified with a superposed tilde, e.g., $\tilde{H} = H/D$). We first consider the footwall as external to the studied domain. A comparison with the finite difference results of *Gonzáles et al.* [2008] is also proposed. In section 3.4, the stress history in the footwall and the stress trajectories in the flat and the hanging wall are presented.

3.1. Folding Without Relief Buildup

[26] The length of the flat is set to D in this example, corresponding to zero shortening ($\delta = 0$). The mesh is presented in Figure S1 of the auxiliary material and is composed of 7530 nodes and 9920 elements.

[27] Maps of the distance to failure for different values of the friction angle ϕ_R over the ramp are presented in Figure 6. Regions of dark blue are exactly at failure. Two regions of failure in the bulk are found for $\phi_R = 5°$, 15° and 20°, for which the whole décollement and the ramp are activated

Table 3. Definition, Dimension and Value Selected for the Parameters of Fault-Bend Fold

Definition	Dimension	Value
Length D	km	4.25
Height H	km	1.
Mass density ρ	kg/m^3	2200.
Gravity acceleration g	m/s^2	9.81
Dip of the ramp γ	deg	30.
Friction angle in the bulk ϕ_B	deg	30.
Cohesion in the bulk c_B	MPa	1.
Friction angle of the décollement ϕ_D	deg	5.
Cohesion of the décollement c_D	MPa	0
Friction angle of the ramp ϕ_R	deg	variable
Cohesion of the ramp c_R	MPa	0
Friction angle of upper flat $\phi_U = \phi_R$	deg	variable
Cohesion of upper flat $c_U = c_R$	MPa	0

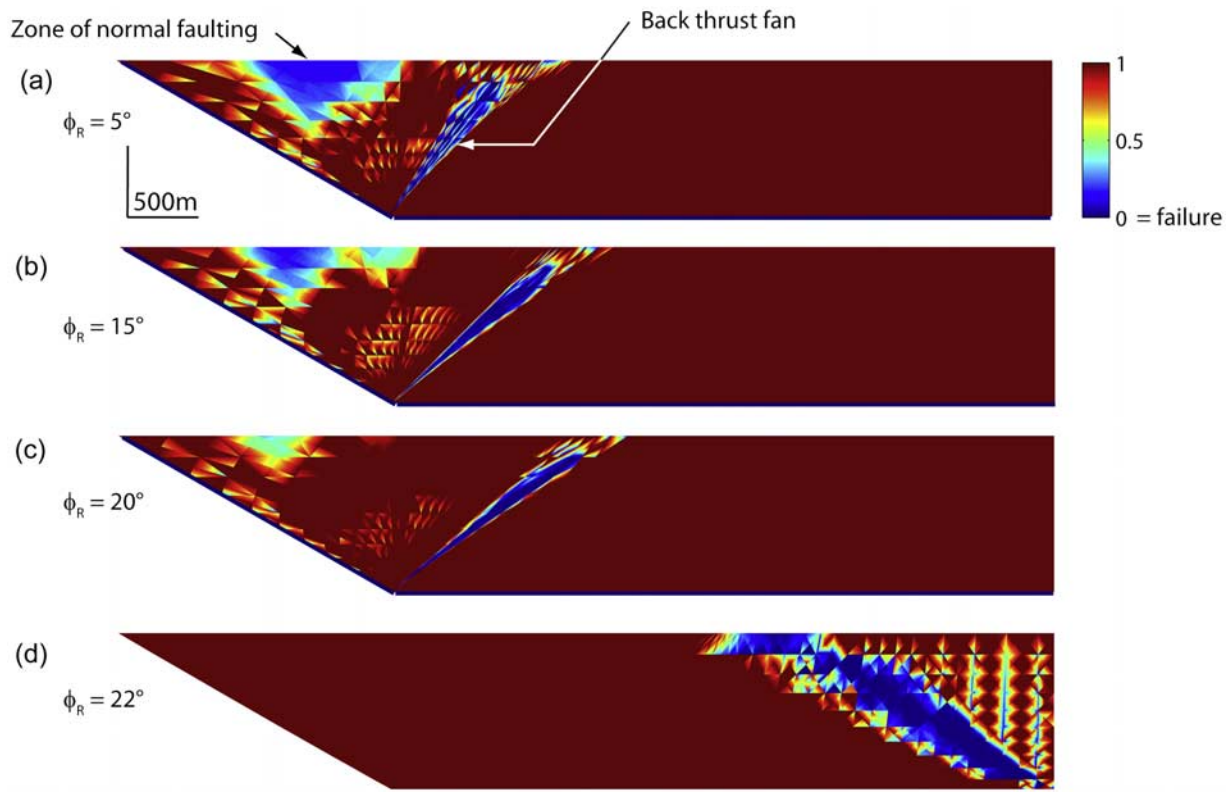

Figure 6. Failure modes for the fault-bend fold without relief buildup, for values of the friction angle over the ramp ϕ_R, as revealed by the scaled distance to Coulomb's criterion π_B, defined in Figure 2 and equation (12) of (a) 5°, (b) 15°, (c) 20°, and (d) 22°. The blue lines along the ramp and décollement mark their activation.

(see blue segments). The first region is the transition between the hanging wall and the flat, the back thrust. We observe that it is not a sharp discontinuity but a narrow fan. This shape is of course mesh sensitive but persists as the mesh is refined so that several elements are present within the blue region. The second main region of failure for ϕ_R = 5°, 15° and 20° is in the hanging wall. It is of smaller extent for larger ϕ_R. This region is, as it will be seen next, where the σ_{xx} stress component is close to zero. It thus corresponds to a region where failure is by normal faulting. Such failure mode was predicted by *Yin* [1993] using Hafner stress type of construction. For ϕ_R = 22° this region of extension does no exist. Furthermore, the ramp and the décollement are not activated and a new failure region occurs at the back, dipping at approximately 30°. This orientation is consistent with the $\pi/4 - \phi_B/2$ angle expected for failure under compression with ϕ_B = 30°. It is thus predicted that a new ramp is formed at the back of the flat, at the contact to the back wall. This transition, between ϕ_R = 20° and 22°, is of course sensitive to the décollement friction angle set to 5°. The transition occurs for ϕ_R less than 15° if ϕ_D is set to 10°, as can be seen in Figure S2 in the auxiliary material.

[28] The dips of the fans for ϕ_R = 5°, 15° and 20°, decrease with the ramp friction. This was predicted by *Maillot and Leroy* [2003] and by *Cubas et al.* [2008]. A quantitative comparison is proposed in Figure 7b where it is seen that the difference between the EEM predictions and those of the kinematics approach are at most of 3°. The EEM solution is presented there with an error bar since defining the central line through the fan is not accurate. This variation of the back thrust dip with the ramp friction angle was validated in the laboratory with sand box experiments [*Maillot and Koyi*, 2006] and the relevance of the predictions to interpret field observations further discussed by *Koyi and Maillot* [2007]. The comparison of our results with the predictions of the kinematics approach of *Cubas et al.* [2008], central to the validation of our implementation of the EEM, is completed by presenting the predicted tectonic forces, normalized by $\rho g D^2$, as a function of the friction angle over the ramp in Figure 7a. The upper bound of the kinematics approach differs from the lower bound of the EEM by less than 1%. Therefore, the exact tectonic force is determined by the limit analysis to within one per cent.

[29] The stress distribution over the fault-bend fold without relief build up is presented in Figure 8. The largest stress values in highly localized regions are cutoff from the ranges of the color bars. The σ_{xx} stress gradient with depth is linear at the back wall, consistent with the applied boundary conditions. It is approximately three times the lithostatic gradient (21.6 MPa/km). In the hanging wall, the horizontal stress is much larger close to the base of the ramp. There are two regions of stress concentration. Region 1 has the shape of a thin lobe emanating from the ramp base and oriented at, approximately, 5° from the ramp. Region 2 is wider and terminates at the boundary of the back thrust. Another interesting feature of the horizontal stress in the hanging wall is that it is close to zero in a large triangular region (dark red) to the left of the root of the ramp and reaching the

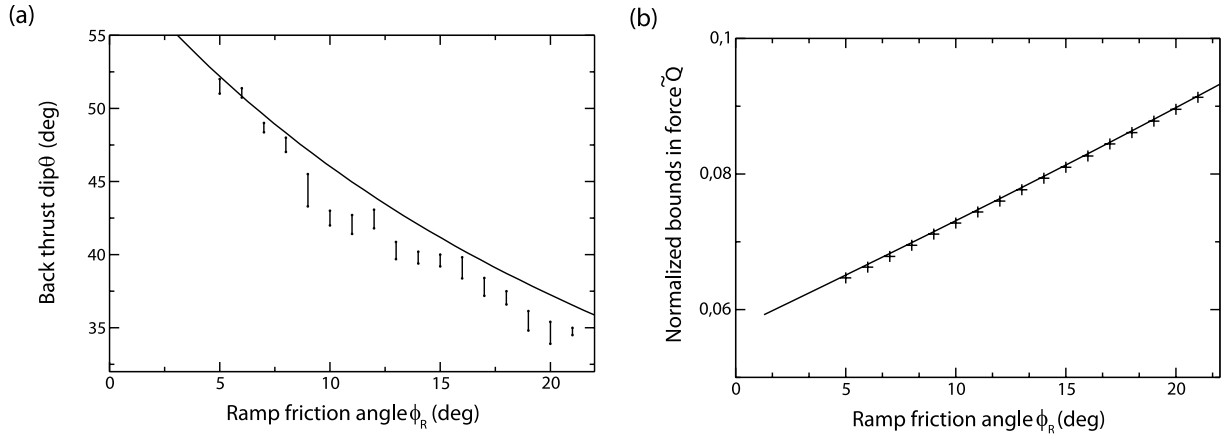

Figure 7. Comparison of (a) the tectonic force and (b) the dip of the back thrust (fan or discontinuity) between the EEM (crosses) and the kinematics approach (continuous curves). The estimates of the average fan dip obtained with the EEM are indicated with error bars.

top surface. This is the region close to failure in extension discussed above. The vertical stress (Figure 8, middle) has the expected lithostatic gradient over most of the flat. In the hanging wall, the maximum vertical stress is nearly twice as large as the lithostatic stress. The larger values are found again in the same two regions of concentration. The shear stress (Figure 8, bottom) is basically zero in most of the back stop in view of the low friction angle over the décollement. The stress state is thus approximately Andersonian in that region (horizontal and vertical directions are principal stress directions). The shear stress has strong gradients in the hanging wall which are positioned again within the two regions of concentration defined for σ_{xx}. The sign of the stress in those regions are consistent with the direction of shear expected in the back thrust and along the ramp. The lobe of stress concentration dipping at 5° from the ramp indicate a potential secondary ramp, conjugate to the back thrust. This interpretation is confirmed by setting the ramp dip at 35°, exactly in the direction of this lobe. The failure mode (Figure S3 in the auxiliary material) is then composed solely of the narrow fan defining the back thrust. The lobe oriented off the original ramp is not present. This remark is part of the wider problem on the activation of existing ramps versus creation of new thrusts, discussed by *Maillot et al.* [2007] analytically and experimentally. Here, the lobes are another expression of the capacity of the EEM to detect new potential thrusting.

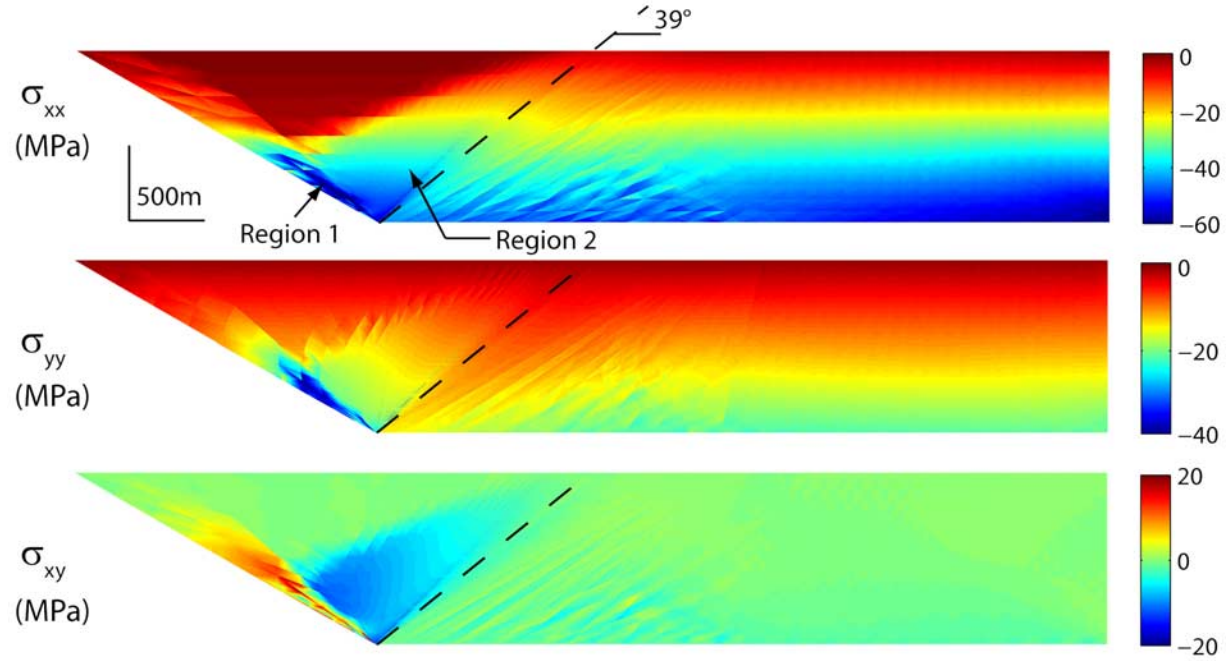

Figure 8. Stress distribution over the hanging wall and the flat for the fully eroded fault-bend fold (unit of MPa). The ramp friction angle is $\phi_R = 15°$. The dashed line shows the central direction of the back thrust defined by the failure fan in Figure 6.

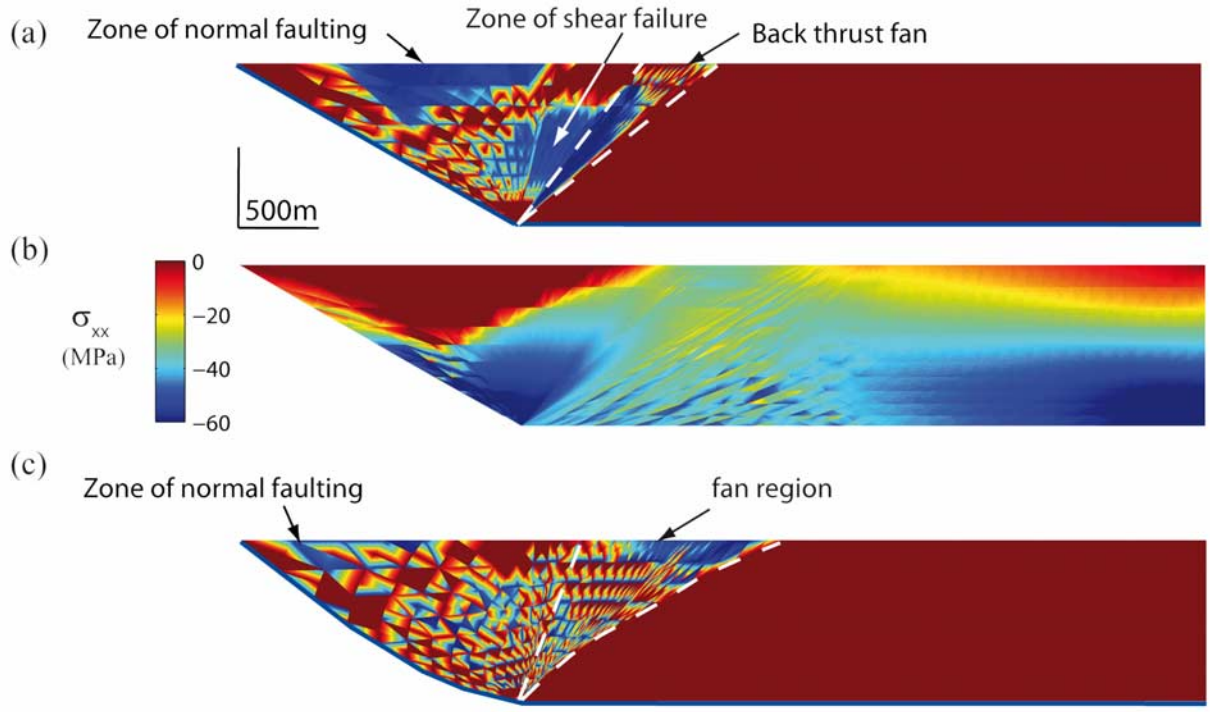

Figure 9. (a) The distribution of the scaled distance to the criterion and (b) the distribution of σ_{xx} for a bulk cohesion c_B of 10 MPa. (c) The distribution of the failure region is less localized and the fan boundary with the flat is also curvy in the presence of a curved ramp, for a bulk cohesion c_B of 1 MPa.

[30] As a final remark, it should be mentioned that the stress analysis above points to a large mean stress P (defined as $(\sigma_{xx} + \sigma_{yy})/2$ and interpreted from Figure 8 (top and middle)) close to the ramp and in the back thrust, and to low values in the hanging wall above the back thrust. Consequently, one should observe fluid flows from the flat toward the back thrust and within the hanging wall away from the two regions of stress concentrations. These flows, not accounted for in our modeling, could have consequences on the material rheology.

3.2. Comparison With Finite Difference Predictions

[31] This first example of folding gives us the opportunity to compare the merits of the EEM with respect to the finite difference method. This comparison is based on the study of *Gonzáles et al.* [2008] of the tensile discontinuities observed in the hanging wall of the Chuculay Fault System, northern Chile. Their numerical simulations are based on a prototype which is rather close to the one considered for this first fold example. The ramp is predefined as a weak zone of finite thickness (500 m) dipping at 50° and ours is discrete with a dip of 30°. The constitutive relations are similar in the two contributions since Coulomb materials are assumed although the zero dilatancy and the elasticity considered by *Gonzáles et al.* [2008] are not necessary for the EEM. We have kept our flat thickness of 1 km, whereas *Gonzáles et al.* [2008] considered 3 and 6 km. We checked that the scaling from 1 to 3 km leads to the scaling of the extent of the zone of tensile failure in the same ratio. No relief is considered here and its consequence will be, however, discussed as well in section 3.3. Four comparisons are now considered with simulations M1, M5, M3, and M4 of *Gonzáles et al.* [2008], referred to as the comparison paper.

[32] The results of their M1 simulation is comparable to the results in Figure 6 for $\phi_R = 5°$ and $\phi_R = 15°$ since their ϕ_R is set to 10°. The shape of the zone of low equivalent shear stress [*Gonzáles et al.*, 2008, Figure 12c] does compare to the our distribution of the stress in the hanging wall. The strain localization of their back thrust is not sufficiently resolved to be compared to the fan predicted here. There is, however, a major difference between these two sets of results: our ramp dips at 30° and their at 50°. It was shown above that increasing the ramp dip from 30° to 35° leads to more compression in the hanging wall and was sufficient to suppress the tensile zone of fracture. A dip of 50° produces the same results. Consequently, only the main difference between our prototype and simulation M1, the presence of a relief in the latter case, can explain the absence of tensile failure zone. It appears from Figure 12e of *Gonzáles et al.* [2008] that the depth of the extension zone is approximately equal to the maximum topography (277 m). This zone is exactly next to the shear zone. In the absence of relief, it is believed that no extension would have been predicted by *Gonzáles et al.* [2008]. The second comparison is with their M5 simulation in which c_B is set to 10 MPa [*Gonzáles et al.*, 2008, Figure 16b]. The same conditions have been considered to produce Figures 9a and 9b for a flat thickness of 1 km and a ramp dip of 30°. We still have a reasonable zone of normal faulting in view of the scaled distance to the criterion and of the distribution of σ_{xx}. Note that the σ_{xx} is much more compressive then in Figure 8 in the hanging wall close to the back thrust

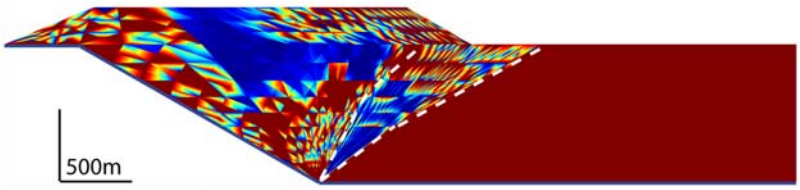

Figure 10. Failure mode in the fault-bend fold with relief buildup, revealed by the distribution of the scaled distance to the Coulomb's criterion π_B (equation (12)). The friction angle over the ramp is $\phi_R = 5°$ and the shortening $\delta = 750$ m. The color code is the same as in Figure 6: dark blue regions tend to reach failure. The blue segments mark the activation of the interfaces.

fan and across this fan, close to the surface. Furthermore, a new region of shear failure is clearly seen in Figure 9a next to the back thrust fan. These results are different from those of *Gonzáles et al.* [2008], who noticed a reduction in the extent of the normal failure zone, certainly due to the relief again. The third comparison is with their M3 simulation [*Gonzáles et al.*, 2008, Figure 15b] which introduces a curvature in the ramp. The distribution of the distance to the criterion presented in Figure 9c identifies a small region of normal faulting also present in the comparison paper. Moreover, the back thrust fan is much wider in the presence of the curved ramp suggesting that the strain does not localize in that instance. Note that the boundary of the fan with the flat is also curvy. The same conclusions are reached by *Gonzáles et al.* [2008]. The fourth comparison is with the M4 simulation for which ϕ_R is set to 25°. They observe no normal faulting within the hanging wall, and we claim that their results correspond to the case presented in Figure 6 for $\phi_R = 22°$. The décollement and the predefined ramp are not activated, and the deformation should take place close to the back wall.

3.3. Folding With Relief Buildup

[33] In this second example, relief builds up (Figure 5b). The shape of the relief was constructed for shortenings δ of 400 and 750 m, with the kinematics approach [*Cubas et al.*, 2008] using the parameters in Table 3, with $\phi_R = 10°$. We will determine the stress distribution within the fold, first for $\delta = 750$ m and $\phi_R = 5°$, then for $\delta = 400$ m and $\phi_R = 7°$. In the second case, we will also determine the stress distribution in the footwall of the fold. The reason for choosing different values of the ramp friction angle will be explained at the end of the section. The mesh is composed to 8586 nodes and 11322 elements, as shown in Figure S5 of the auxiliary material.

[34] The failure mode is presented in Figure 10 for $\delta = 750$ m. The two major regions of failure found in the absence of relief are still present. The first is the back thrust which has the shape of a fan wider than in the first example. Failure occurs approximately uniformly in the lower part of the fan close to the root to the ramp. In the upper part, failure is localized into a series of oblique rays that could indicate distributed faulting. Furthermore, the fan rotates from the lower to the upper part toward lesser dips. It is approximately 55° in the lower part, consistent with the 53° found in Figures 6 and 7b. It means that close to the root of the ramp, the influence of the relief is minor. To the contrary, in the upper part of the structure, failure is influenced by the relief. The second main region of failure is in the hanging wall. It corresponds to the zone of extension described for the first example and it now extends to the relief. Failure in extension occurs over more than 50% of the hanging wall thickness measured from the free top surface to the root of the ramp. This distribution of failure has to be complemented, for larger ϕ_R (7° is considered in Figure S6 of the auxiliary material). In that case, near half of the flat, next to the back thrust, is also close to failure.

[35] These results differ from those of *Gonzáles et al.* [2008] in at least two ways. First, the depth of the tensile fracture zone is deeper here because of the low dip of our ramp. Second, the bending of the topographic surface in the comparison paper is due essentially to the absence of thrusting over the upper flat because of the continuity assumption implied by the numerical scheme. The simplified geometrical construction of *Cubas et al.* [2008] has been helpful in relaxing this constraint and provides a partial collapse of the hanging wall over of the upper flat. The region of normal faulting is then found further away from the ramp closer to the point on the topography which is on top on the root of the ramp.

[36] The last example is for a shortening $\delta = 400$ m and accounting for the footwall. The stress distribution within the flat (Figure 11) is similar to the one obtained in the absence of relief, Figure 8. Note that the maxima are larger from those discussed earlier although the friction on the ramp is less, because of the highly localized stress within the lobe pending at a few degrees from the ramp. Four comments are in order regarding the footwall. First, there is no failure there. Second, the horizontal stress has a smaller gradient with depth than in the flat region. This decrease of the horizontal forces is explained by the overall equilibrium of the structure and the presence of the resisting shear over the whole décollement. Third, the vertical stress gradient in the footwall is controlled by gravity and thus not affected by the ramp. The shear stress is in general small compared to the magnitude of the two other stresses so that Andersonian conditions prevail, approximately. Fourth, important stress concentrations are observed close to the root of the ramp despite the absence of any failure.

[37] The EEM also predicts the maximum relief attainable prior to the transfer of activity from the predefined ramp to the back wall where the emergence of a new ramp takes place. This transfer is easily explained using the analogy with the influence of the ramp friction angle in the absence of relief: there is a maximum friction of 21° at which the proposed ramp is abandoned in favor of the new ramp (Figure 6d). Similarly, with gradual relief build up, after a

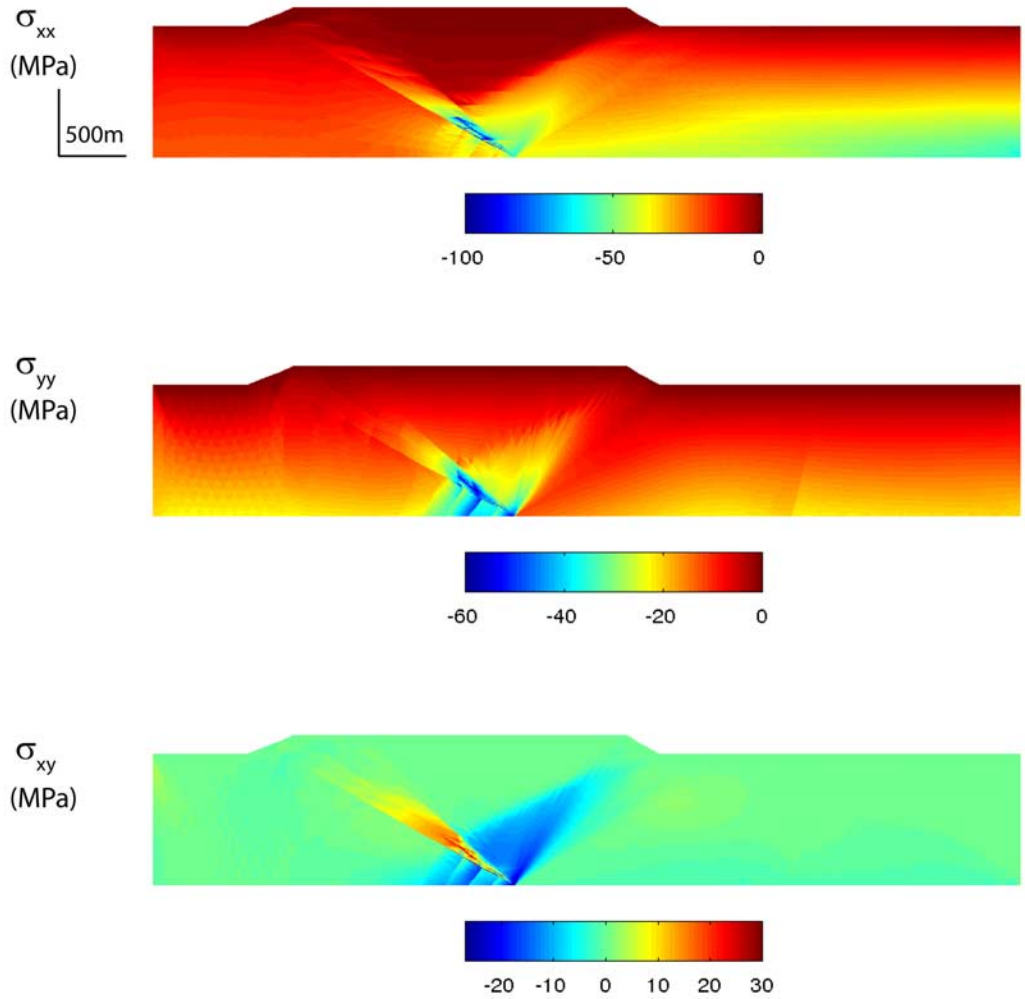

Figure 11. Stress distribution over the whole fold including the foot wall (unit: MPa), for $\phi_R = 7°$ and a shortening $\delta = 400$ m.

shortening of less than 750 m for $\phi_R = 10°$, for example, the proposed ramp is abandoned and the new thrust initiates in the flat, at the back wall boundary. Since we were interested by the stress distribution around the fold, we set low enough ϕ_R.

3.4. Stress Histories and Trajectories

[38] The computations reported so far are history-independent. A chronology is only implicit through the amount of shortening imposed at the back wall. This succession of independent results is now used to study stress histories, thus shedding light on the evolution of the stress state during the kinematic sequence of thrusting determined by *Cubas et al.* [2008].

[39] We first examine stress histories at fixed positions in the foot wall. The dimensionless equivalent shear and mean stresses (9), are presented as functions of the shortening at five locations indicated by solid dots (Figure 12). Point 5 is approximately at 100 m from the ramp and this distance decreases linearly with depth to be only of 10 m for point 1. The depth of points 1 to 5 are approximately 850, 650, 450, 250, and 50 m. The gradient in the equivalent shear stress is strong close to the root of the ramp with a ratio of four, approximately between the stress at points 1 and 2. The relief build up does not change significantly this ratio and the important parameter is thus the distance to the root of the ramp. The mean stress is also strongly dependent on this distance but its magnitude increases linearly with the shortening because of the added weight of the relief acting on the ramp. Note that point 5 exhibits a larger increase in σ_e with shortening probably resulting from the sliding of the growing forelimb above it. One could now imagine the evolution of the stress during a sequence of normal thrusting where the dashed line is the abandoned ramp and the new ramp the parallel is the solid line (Figure 12a). Point 5′ would first undergo the stresses just described for point 5, followed by the extensional regime in the back wall (Figure 10).

[40] Next, we examine the stress along material trajectories (ξ axis in Figure 13a). In view of the minor influence of the relief, we concentrate on the fold with erosion. The trajectories provide the stress histories of a convected material point. The point initially at the back wall ($\xi = 0$) is translated parallel to the décollement and changes direction at the crossing of the back thrust, idealized as a sharp discontinuity, to move up parallel to the ramp. It reaches the surface between $\xi = 4.7$ and 5.7 km, depending on the depth

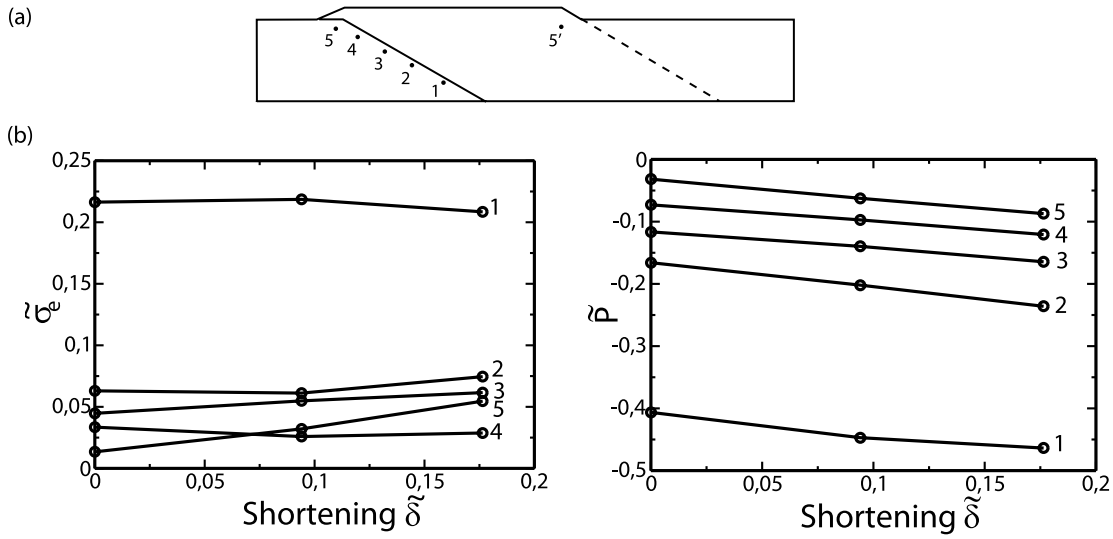

Figure 12. (a) Definition of the five different locations in the footwall. (b) The history of the dimensionless, equivalent shear stress $\tilde{\sigma}_e$, and mean stress $\tilde{P}$ at five different locations in the footwall.

η of the trajectory, and is eroded away. The equivalent shear and mean stresses along those trajectories are presented in Figure 13b. The trajectory passes through various elements of the mesh and the stress at the node closest to the ξ axis has been used to construct Figures 13a and 13b, explaining the oscillations. Three depths are considered corresponding to 0.5, 0.75 and 0.85 times the height H. In most of the flat, the magnitude of the equivalent shear and mean stress decreases before arriving within the vicinity of the back thrust. Within the back thrust ($\xi \approx 4$ km), the equivalent shear stress first increases to a value close to the one found at the back wall before sustaining a sharp drop. The rest of the decrease during the uplift in the hanging wall is then marginal compared to that drop. The mean stress displays the same tendencies: the decrease in magnitude registered over the flat accelerates when arriving close to the back thrust. Sharp, opposite gradients of the magnitude are found inside the back thrust zone, followed by a linear decrease to zero toward the surface.

4. Conclusion

[41] The objective of this paper was to demonstrate that the equilibrium element method (EEM) provides estimates of the stress distribution, the tectonic force, the shape and the position of the failure mechanisms at any given stage in the development of a geological structure. It requires only the spatial distribution of the rock strength, defined in this

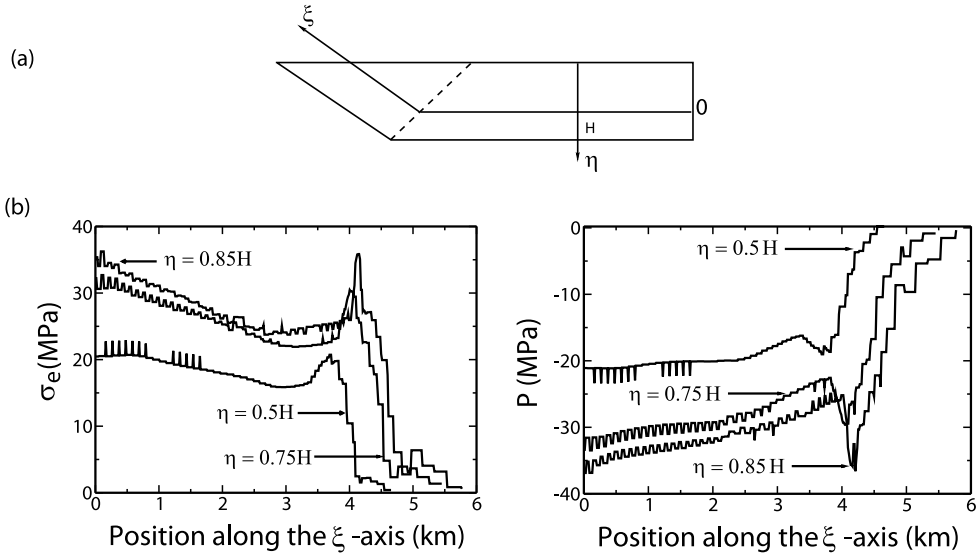

Figure 13. (a) Definition of the trajectory ξ and the depth η in the back stop. (b) The mean stress P and the equivalent shear stress σ_e (unit of MPa), along the trajectory ξ (unit of km) at depth η in the back stop for $\phi_R = 15°$.

paper by the Coulomb criterion, without any further assumptions on the rheology.

[42] The EEM implementation is first validated with Hafner's problem. The tectonic force predicted with the EEM meets the analytical solution up to machine precision. Failure occurs by décollement slip or bulk failure, those two modes being concomitant only exceptionally. Consequently, we question the derivation of the local fracture orientation in the bulk from the stress state necessary to activate the décollement, as proposed by *Hafner* [1951]. Indeed, the EEM predicts rather different stress states for bulk failure versus basal slip.

[43] The EEM is then applied to two fault-bend folds, the first without relief build up and the second accounting for the formation of a relief. It predicts the formation of a back thrust in the form of a narrow fan rooted at the base of the ramp. The fan dip is controlled by the ramp and bulk frictions as predicted by *Cubas et al.* [2008] and varies with depth in the presence of a relief and the curvature of the ramp. For certain ramp friction and dip, a zone of normal faulting appears at the surface in the hanging wall. These results are partly in agreement with and provide a new interpretation of some of the finite difference predictions of *Gonzáles et al.* [2008], who considered a complete elastic-plastic constitutive relation. No failure is detected in the footwall for the two folds and for the range of parameters selected.

[44] The optimum stress state for the two folds is mostly controlled by the concentration originating from the root of the ramp on the décollement and the presence of the back thrust. The in-plane mean stress and the equivalent shear stress sustain sharp variations prior to the entrance and at the exit of the back thrust, as one moves from the flat to the hanging wall.

[45] Applied to Nankai accretionary wedge (in the auxiliary material), the EEM reveals the complexity of the potential failure mechanism, composed of two parallel back thrusts or two subparallel ramps. Its high sensitivity to variations in the décollement friction angle and to the details of the surface topography are consistent with a wedge close to criticality, as defined by *Dahlen* [1984] and *Lehner* [1986]. It is also shown that the position of the currently active ramp cannot be selected as a failure mechanism with the assumption of uniform properties suggesting, as by *Cubas et al.* [2008], that the active ramp is weaker than the bulk material.

[46] The EEM is complementary to the kinematics approach of limit analysis, central to *Cubas et al.*'s [2008] study, since the two methods provide the largest lower bound and the least upper bound, respectively, to the exact unknown tectonic force. The EEM, because of the systematic spatial discretization, leads to a large number of degrees of freedom whereas the kinematics approach is often restrained to a small number of degrees of freedom. This application of the EEM thus provides an error estimate on the tectonic force and validates the selection of the failure mechanisms done with the kinematics approach. The extension of limit analysis to evolving geological structures could be conducted asymmetrically: the kinematics approach applied to thrusting sequences [*Cubas et al.*, 2008] is central to control the evolution problem whereas the statics approach, at the basis of the EEM, is only used to define the stress field at any stage of the fold development and to check the error in tectonic force. Also, since no rheology is used apart from the Coulomb criterion, the EEM cannot predict the geometry at failure for materials exhibiting large elastic or viscous deformation prior to failure.

[47] The results of the EEM have merits on their own and two potential directions of future developments are now discussed. First, the computations presented in this contribution show clearly that there is a gradient in the mean stress in the presence of a ramp close to the back thrust. This gradient may be the driving force for fluid flow. Such fluid flows could be studied in the laboratory with appropriately scaled analogue materials [*Mourgues and Cobbold*, 2003] or could also be predicted by numerical means. In both instances, the fluid pressure distribution could be accounted for in the EEM by recourse to strength limit criteria based on effective stress measures. The combined approach, fluid flow and EEM, should be applied to accretionary wedges where the influence of the fluids on the deformation has been recognized [*Le Pichon et al.*, 1993] to understand fault orientations and failure mechanisms. The second direction of developments concerns the study of the interseismic period. The EEM could provide the stress distribution during the restrengthening of the ruptured faults. In particular, it could provide the stress distribution between en echelon rupture surfaces, as in Landers area, California [*Peltzer et al.*, 1996; *Olsen et al.*, 1997], avoiding the stress singularities typically predicted with the assumption of linear elasticity. Similarly, in fold-and-thrust belts with multiple fault systems, it is hoped that the EEM could predict the most likely fault to be active.

[48] In summary, the EEM should provide new means to study stress distributions under static conditions, with a limited number of assumptions on the material properties, with a vast domain of applications, ranging from folding development in fold-and-thrust belts, accretionary wedges, sedimentary basins, to the interseismic fault recovery.

[49] **Acknowledgments.** This paper benefited at different stages of it submission from comments of S. Buiter, Geological Survey of Norway, Trondheim; of M. Cooke, University of Massachusetts, Amherst; and of an anonymous reviewer. They are all sincerely thanks for their advice which helped us in preparing the final version.

References

Buiter, S. J. H., A. Y. Babeyko, S. Ellis, T. V. Gerya, B. J. P. Kaus, A. Kellner, G. Schreurs, and Y. Yamada (2006), The numerical sandbox: comparison of model results for a shortening and an extension experiment, in *Analogue and Numerical Modelling of Crustal-Scale Processes*, edited by S. J. H. Buiter and G. Schreurs, *Geol. Soc. Spec. Publ.*, *253*, 29–64.

Cubas, N., Y. M. Leroy, and B. Maillot (2008), Prediction of thrusting sequences in accretionary wedges, *J. Geophys. Res.*, *113*, B12412, doi:10.1029/2008JB005717.

Dahlen, F. A. (1984), Noncohesive critical Coulomb wedges: An exact solution, *J. Geophys. Res.*, *89*, 10,125–10,133.

Erickson, S. G., and W. R. Jamison (1995), Viscous-plastic finite-element models of fault-bend folds, *J. Struct. Geol.*, *17*, 561–573.

Erickson, S. G., L. M. Strayer, and J. Suppe (2001), Initiation and reactivation of faults during movement over thrust-fault ramp: Numerical mechanical models, *J. Struct. Geol.*, *23*, 11–23.

Gonzáles, G., M. Gerbault, J. Martinod, J. Cembrano, D. Carrizo, R. Allmendinger, and J. Espina (2008), Crack formation on top of propagating reverse fauls of the Chuculay Fault System, northern Chile: Insights from field data and numerical modelling, *J. Struct. Geol.*, *30*, 791–808.

Hafner, W. (1951), Stress distributions and faulting, *Geol. Soc. Am. Bull.*, *62*, 373–398.

Hill, R. (1950), *The Mathematical Theory of Plasticity*, Oxford Univ. Press, Oxford, U. K.

Koyi, H. A., and B. Maillot (2007), Tectonic thickening of hanging wall units over a ramp, *J. Struct. Geol.*, *29*, 924–932.

Krabbenhøft, K., A. V. Lyamin, and S. W. Sloan (2007), Formulation and solution of some plasticity problems as conic programs, *Int. J. Solids Struct.*, *44*, 1533–1549.

Lehner, F. K. (1986), Comments on ''Noncohesive critical Coulomb wedges: An exact solution,'' *J. Geophys. Res.*, *91*, 793–796.

Le Pichon, X., P. Henry, and S. Lallemant (1993), Accretion and erosion in subduction zones: The role of fluids, *Annu. Rev. Earth Planet. Sci.*, *21*, 307–331.

Leroy, Y. M., and N. N. Triantafyllidis (2000), Folding and localized faulting in a frictional, cohesive overburden resting over a viscous substratum, in *Aspects of Tectonic Faulting*, edited by F. K. Lehner and J. L. Urai, pp. 109–139, Springer, Heidelberg, Germany.

Maillot, B., and H. Koyi (2006), Thrust dip and thrust refraction in fault-bend folds: analogue models and theoretical predictions, *J. Struct. Geol.*, *28*, 36–49.

Maillot, B., and Y. M. Leroy (2003), Optimal dip based on dissipation of back thrusts and hinges in fold-and-thrust belts, *J. Geophys. Res.*, *108*(B6), 2320, doi:10.1029/2002JB002199.

Maillot, B., and Y. M. Leroy (2006), Kink-fold onset and development based on the maximum strength theorem, *J. Mech. Phys. Solids*, *54*, 2030–2059.

Maillot, B., C. Barnes, J.-M. Mengus, and J.-M. Daniel (2007), Constraints on friction coefficients by an inverse analysis of sand box thrust dips, *J. Struct. Geol.*, *29*, 117–128.

Mourgues, R., and P. R. Cobbold (2003), Some tectonic consequences of fluid overpressures and seepage forces as demonstrated by sandbox modelling, *Tectonophysics*, *376*, 75–97.

Odé, H. (1960), Faulting as a velocity discontinuity in plastic deformation, in *Rock Deformation*, edited by D. Griggs and j. Handin, *Mem. Geol. Soc. Am.*, *79*, 293–321.

Olsen, K., R. Madariaga, and R. Archuleta (1997), Three dimensional dynamic simulation of the 1992 Landers earthquake, *Science*, *278*, 834–838.

Ortiz, M., Y. Leroy, and A. Needleman (1987), A finite element method for localized failure analysis, *Comput. Methods Appl. Mech. Eng.*, *61*, 189–214.

Peltzer, G., P. Rosen, F. Rogez, and K. Hudnut (1996), Postseismic rebound in fault step-overs caused by pore fluid flow, *Science*, *272*, 1202–1204.

Rudnicki, J. W., and J. R. Rice (1975), Condition for the localization of deformation in pressure-sensitive dilatant materials, *J. Mech. Phys. Solids*, *23*, 371–394.

Salençon, J. (1974), *Théorie de la plasticité pour les applications à la mécanique des sols*, Eyrolles, Paris. (English translation, *Applications of the Theory of Plasticity in Soil Mechanics*, John Wiley, Chichester, U. K., 1977).

Salençon, J. (2002), *De l'élasto-Plasticité au Calcul à la Rupture*, École Polytech., Palaiseau, and Ellipses, Paris.

Sciamanna, S., W. Sassi, R. Gambini, J. L. Rudkiewicz, F. Mosca, and C. Nicolai (2004), Predicting hydrocarbon generation and expulsion in the southern Apennines Thrust Belt by 2D integrated structural and geochemical modeling: Part I - Structural and thermal evolution, in *Deformation, Fluid Flow, and Reservoir Appraisal in Foreland Fold and Thrust Belts*, edited by R. Swennen, F. Roure, and J. W. Granath, pp. 51–67, AAPG, Tulsa, Okla.

Souloumiac, P., and A. Modaressi (2008), Comparison between Finite Element Method and Equilibrium Element Method to predict stress field in fault-bend folds, paper presened at 12th International Conference of the International Association for Computer Methods and Advances in Geomechanics, Goa, India.

Suppe, J. (1983), Geometry and kinematics of fault-bend folding, *Am. J. Sci.*, *283*, 7, 684–721.

Timoshenko, S. P., and J. N. Goodier (1934), *Theory of Elasticity*, McGraw-Hill, New York.

Yin, A. (1993), Mechanics of wedge-shaped fault blocks 1. An elastic solution for compressional wedges, *J. Geophys. Res.*, *98*, 14,245–14,256.

Zoetemeijer, R., and W. Sassi (1992), 2D reconstruction of thrust evolution using the fault-bend fold method, in *Thrust Tectonics*, edited by K. McClay, pp. 133–140, Chapman and Hall, London.

K. Krabbenhøft, Centre for Geotechnical and Materials Modeling, University of Newcastle, Callaghan, NSW 2308, Australia. (Kristian.Krabbenhoft@newcastle.edu.au)

Y. M. Leroy, Laboratoire de Géologie, CNRS, École Normale Supérieure, 24 rue Lhomond, F-75231 Paris CEDEX 05, France. (leroyy@geologie.ens.fr)

B. Maillot, Département Géosciences Environnement, Université de Cergy-Pontoise, 33 boulevard du Port, F-950111 Cergy-Pontoise CEDEX, France. (bertrand.maillot@u-cergy.fr)

P. Souloumiac, Laboratoire MSS-Mat, CNRS, École Centrale Paris, Grande Voie des Vignes, F-92295 Châtenay Malabry CEDEX, France. (souloumiac@geologie.ens.fr)